Available online at www.sciencedirect.com
ScienceDirect
Trans. Nonferrous Met. Soc. China 30(2020) 1904−1915
Transactions of Nonferrous Metals Society of China
www.tnmsc.cn

Enhancement of lithium storage capacity and rate performance of Se-modified MnO/Mn_3O_4 hybrid anode material via pseudocapacitive behavior

Lie-wu LI[1], Li-ping WANG[1,2], Ming-yu ZHANG[1], Qi-zhong HUANG[1], Ke-jian HE[3], Fei-xiang WU[4]

1. State Key Laboratory of Powder Metallurgy, Central South University, Changsha 410083, China;
2. College of Biological and Environmental Engineering, Changsha University, Changsha 410022, China;
3. Advanced Research Center, Central South University, Changsha 410083, China;
4. School of Metallurgy and Environment, Central South University, Changsha 410083, China

Received 3 October 2019; accepted 28 May 2020

Abstract: To improve rate and cycling performance of manganese oxide anode material, a precipitation method was combined with thermal annealing to prepare the $MnO/Mn_3O_4/SeO_x$ (x=0, 2) hybrid anode by controlling the reaction temperature of Mn_2O_3 and Se powders. At 3 A/g, the synthesized $MnO/Mn_3O_4/SeO_x$ anode delivers a discharge capacity of 1007 mA·h/g after 560 cycles. A cyclic voltammetry quantitative analysis reveals that 89.5% pseudocapacitive contribution is gained at a scanning rate of 2.0 mV/s, and the test results show that there is a significant synergistic effect between MnO and Mn_3O_4 phases.

Key words: lithium-ion battery; manganese oxide; anode material; pseudocapacitive behavior; synergistic effect

1 Introduction

The development of the high-performance lithium-ion batteries (LIBs) is driving the progress of portable and ubiquitous electronics [1,2]. The realization of high-performance LIBs requires the electrode materials of high energy and power density, for which the conventional graphite anode material can no longer meet the urgent demands due to its low theoretical capacity (372 mA·h/g) and poor rate capability [3]. By designing nanostructures and combining metal oxide (MO) with carbon materials, both the specific capacity and rate capability of these MO-modified anode materials can be improved significantly [4]. However, the intrinsically poor Li^+ diffusion kinetics in metal oxide anode materials degrades the electrochemical activity. In the process of pseudocapacitance lithium storage, the redox reactions take place reversibly and rapidly at or near the surface of electrode [5], so as to achieve high power density [6].

This kind of pseudocapacitance lithium storage behavior has been reported recently in a number of transition metal oxides (TMOs) anode materials [7,8]. The enhancement of the pseudo-capacitive contribution is considered as one of the most effective ways to improve the rate capability of the TMO anode materials. Of these TMOs, the manganese oxide anode materials have a high pseudocapacitive contribution through reasonable structural design [9,10]. In addition, the manganese oxide anode materials have the advantages of high theoretical lithium storage capacity, low platform voltage, high abundance in natural world,

Foundation item: Project (2018JJ2513) supported by the Natural Science Foundation of Hunan Province, China; Project (18A378) supported by the Education Bureau Research Foundation of Hunan Province, China; Project (2019GK4012) supported by the Emerging Strategic Industrial Science and Technology Project of Hunan Province, China
Corresponding author: Ming-yu ZHANG, Tel: +86-13667385511; E-mail: zhangmingyu@csu.edu.cn
DOI: 10.1016/S1003-6326(20)65349-3

environmental benignity, low price, etc [4]. A previous work found that the phase boundaries are generally rich in lattice defects, distortions, and dislocations, exerting a significant influence on the charge distribution. Benefiting from the abundant phase boundaries, $CoSe_2$/ZnSe exerts a low Na^+ adsorption energy and fast diffusion kinetics for sodium-ion batteries [11]. Selenium (Se) has also been widely considered due to its high electronic conductivity (1×10^{-1} S/cm) and good lithium storage performance [12,13]. Moreover, manganese oxide can be reduced by Se under certain temperature conditions based on thermodynamic calculation. Thus, we can obtain high energy density by means of phase regulation of manganese oxides, and then improve their cycling performance at high current density through stimulating a high pseudocapacitive contribution by surface and internal microstructure evolution. However, no attempts have been made so far to prepare any multi-phase manganese oxide anode materials for LIBs and explore their synergistic effects from these phases.

Herein, we proposed a scalable approach to fabricate the novel Se-modified MnO/Mn_3O_4 hybrid ($MnO/Mn_3O_4/SeO_x$ (x=0, 2)) by thermal annealing of Mn_2O_3 powder with Se powder in order to produce LIBs anode with excellent performance. The residual amount of Se in the hybrid and the good interparticle adhesion are beneficial to the electronic transfer, thus improving the conversion reaction rate and efficiency, whereas the increasing phase boundaries between MnO and Mn_3O_4 can improve the Li^+ storage among the particles, thus accelerating Li^+ diffusion kinetics. In addition, the manganese oxides are transformed from a crystalline state to an amorphous one during the charge/discharge cycles, and this amorphous state can increase the void space in the hybrid for lithium storage. Furthermore, the cyclic voltammetry (CV) tests reveal a high pseudocapacitive contribution for lithium storage.

2 Experimental

2.1 Preparation of $MnO/Mn_3O_4/SeO_x$ hybrid

The Mn_2O_3 powder was prepared according to our previous report [14]. The $MnO/Mn_3O_4/SeO_x$ hybrid was prepared by the method of thermal annealing under a negative pressure. Firstly, 0.5 g Mn_2O_3 and 1 g Se powders were placed at the two ends of a crucible, respectively, which was covered by another crucible. Secondly, the crucibles containing samples were placed in a tube furnace, and the pressure in the tube furnace was controlled to keep a negative pressure by a vacuum pump. Thirdly, the vacuum pump was shut off and then the tube furnace was heated at a heating rate of 5 °C/min up to 650 °C, kept at the temperature of 650 °C for 2 h, and then cooled down to room temperature. Finally, the $MnO/Mn_3O_4/SeO_x$ hybrid was obtained. For comparison, the $Mn_2O_3/Mn_3O_4/SeO_x$ and Mn_3O_4/SeO_x hybrids were also prepared by thermal annealing of the Mn_2O_3 powder with the Se powder under a negative pressure at 500 and 800 °C, respectively.

2.2 Material characterization

X-ray diffraction (XRD) patterns of the samples were measured on Rigaku Dmax/2550VB+ 18 kW instrument to identify the phases in the prepared hybrids. Scanning electron microscope (SEM, FEI Nova Nano SEM230) was adopted to reveal the morphology and to do energy dispersive X-ray (EDX) elemental mapping. Transmission electron microscope (TEM, JEOL JEM−2010) was used to characterize the microstructure. The BET surface areas and pore size distribution were tested on a JW–BK100C instrument. X-ray photo-electronic spectroscopy (XPS) data were obtained by Thermo ESCALAB 250XI instrument using Al K_α radiation.

2.3 Electrochemical testing

A 2032-type coin cell was fabricated using lithium metal as the counter electrode and Celgard 2500 as the separator, and using $LiPF_6$ (1 mol/L) in a mixture of ethylene carbonate (EC) and dimethyl carbonate (DMC) with a volume ratio of 1:1. The working electrodes were prepared by mixing active material, carbon black, and polyvinylidene fluoride (PVDF) in a mass ratio of 7:2:1. The well-mixed slurry was coated on Cu foil, and then dried in a vacuum oven. The mass loading of active materials was 0.8−1.0 mg/cm^2 on circular discs (d=12 mm) of Cu foil. CV analysis was conducted at 0.1−2.0 mV/s within the range of 0.01−3.0 V (vs Li/Li^+) on a CHI760E electrochemical workstation. Cycle life and rate capability of the cells were tested within a voltage window of 0.01−3.0 V (vs

Li/Li^+) by LAND CT2001A analyzer at 25 °C. EIS experiments were carried out using a CHI760E electrochemical workstation in the frequency range of 0.01 Hz−100 kHz.

3 Results and discussion

The synthesis procedure of $MnO/Mn_3O_4/SeO_x$ hybrid involves precipitating, aging, calcining and thermal annealing with Se powder under negative pressure (Fig. 1(a)). Firstly, NaOH and Na_2CO_3 mixed solution was dropwise added into the $MnCl_2$ solution, and a uniform suspension containing $Mn(OH)_2$ and $MnCO_3$ was obtained. After aging, $Mn(OH)_2$ was transformed to $MnO(OH)_2$. Through post-thermal calcination, the Mn_2O_3 powder was obtained [14]. The porous structure was well formed because of the release of CO_2 gas during thermal treatment ($MnO(OH)_2+MnCO_3=Mn_2O_3+H_2O(g)+CO_2(g)$) [15]. Finally, the $MnO/Mn_3O_4/SeO_x$ hybrid was produced by thermal annealing of the Mn_2O_3 with Se powder under a negative pressure (Fig. 1(b)). It is the first time that Se was utilized to control the phase of manganese oxides ($2Mn_2O_3+Se(g)=4MnO+SeO_2(g)$, $6Mn_2O_3+Se(g)=4Mn_3O_4+SeO_2(g)$). The $MnO/Mn_3O_4/SeO_x$ hybrid shows a claybank color, indicating that the main phase of the surface layer of the hybrid should be Mn_3O_4 (Fig. 1(c)).

The SEM images of the $MnO/Mn_3O_4/SeO_x$ hybrid show a distinct feature that the submicron particles are adhered tightly to each other, which is beneficial to reducing the interfacial resistance (Figs. 2(a) and (b)). The elemental mapping images in Figs. 2(c), (d) and (e) demonstrate a uniform distribution of Mn and O. Figure 2(f) shows the EDX analysis results of the surface for the $MnO/Mn_3O_4/SeO_x$ hybrid in Fig. 2(b), which indicate that the mole fraction of Se in the $MnO/Mn_3O_4/SeO_x$ hybrid is 4.34%. The content of Se element is relatively low, so the morphological features of Fig. 2(b) cannot be seen in Fig. 2(e). It is worthy to note that the residual amount of Se in the $MnO/Mn_3O_4/SeO_x$ hybrid can improve its electronic conductivity [16].

The XRD patterns in Fig. 3 reveal that the $MnO/Mn_3O_4/SeO_x$ hybrid is composed of a cubic MnO phase (JCPDS No. 07−0230) and a tetragonal Mn_3O_4 phase (JCPDS No. 24−0734). According to the crystal parameters in the XRD pattern, the microcrystal size of the sample can be calculated by the Debye−Scherrer formula, from which the microcrystalline sizes of the MnO and Mn_3O_4 in the $MnO/Mn_3O_4/SeO_x$ hybrid are 24.0 and 21.8 nm, respectively. The microcrystalline sizes of MnO and Mn_3O_4 are so small that much more grain boundaries can be formed. And these abundant grain boundaries are conducive to increasing the

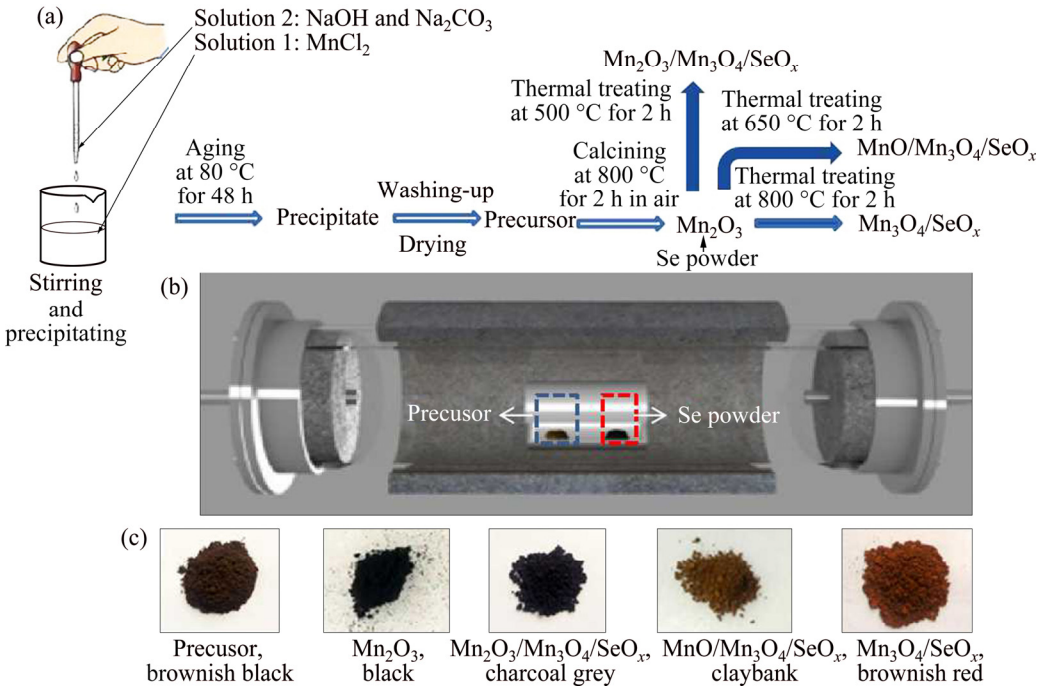

Fig. 1 Schematic illustration of synthesis route for preparing Mn/Se oxide hybrids (a), schematic diagram of equipment for preparing Mn/Se oxide hybrids (b) and photos of obtained hybrids (c)

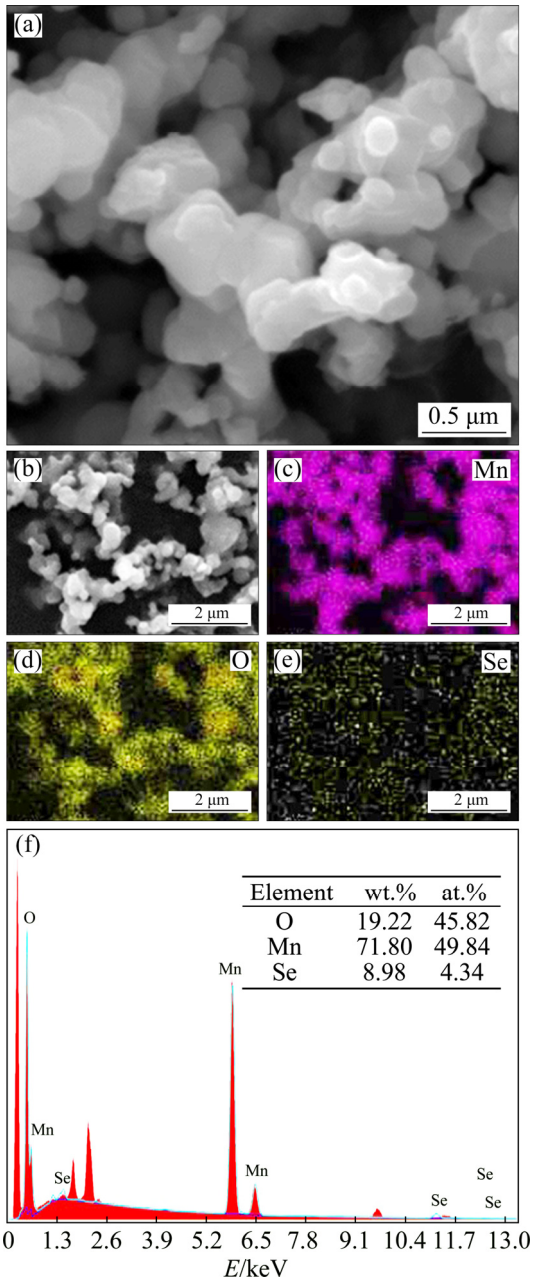

Fig. 2 SEM image of $MnO/Mn_3O_4/SeO_x$ hybrid (a), low magnification image of (a) (b), Corresponding EDX mapping images of (b) for Mn (c), O (d) and Se (e) and corresponding EDX analysis results of Mn, O and Se (f)

diffusion channels for Li^+. The process of materials preparation was performed in a negative pressure airtight environment, resulting in a trace of Se and SeO_2 still remaining in the MnO/Mn_3O_4 composite material, thus the contents of both Se and SeO_2 are below the detection limit of XRD. The XRD patterns of the comparison hybrids (Mn_2O_3, $Mn_2O_3/Mn_3O_4/SeO_x$ and Mn_3O_4/SeO_x) are also shown in Fig. 3.

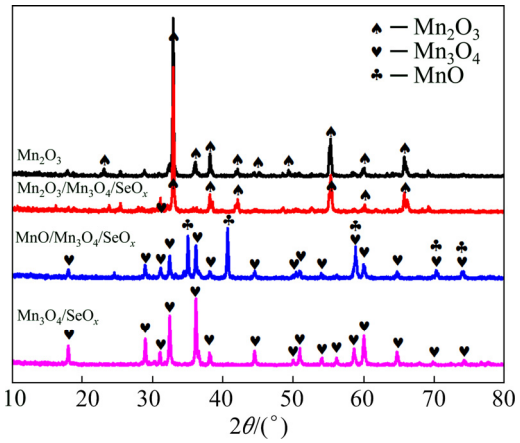

Fig. 3 XRD patterns of different samples

TEM examination was performed to further understand the fine microstructure and crystallinity of $MnO/Mn_3O_4/SeO_x$ hybrid. Figures 4(a) and (b) clearly illustrate the microstructural feature that the submicron particles are adhered tightly to each other. It can also be clearly observed from the high-resolution TEM image in Fig. 4(c) that there are two phases in the $MnO/Mn_3O_4/SeO_x$ hybrid, which is consistent with the XRD results. Furthermore, there is an obvious phase boundary between MnO and Mn_3O_4, which is beneficial to the acceleration of Li^+ diffusion [17]. Figure 4(c) also shows that the

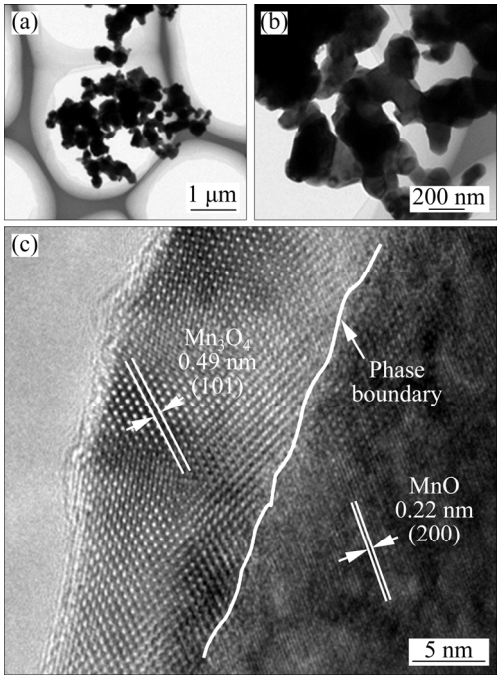

Fig. 4 TEM image of $MnO/Mn_3O_4/SeO_x$ hybrid (a), high-magnification image of (a) (b) and high-resolution image of (b) (c)

main phase in the outer layer (10−15 nm) of the hybrid is Mn_3O_4, confirming the speculation in Fig. 1(c). The electronic conductivity of Mn_3O_4 is 10^{-5}–10^{-6} S/m and that of MnO is 10^{-7} S/m, therefore, the Mn_3O_4 on the surface of the $MnO/Mn_3O_4/SeO_x$ hybrid is conducive to the electron transfer [18].

X-ray photoelectron spectroscopy (XPS) spectra of the Mn_2O_3, $Mn_2O_3/Mn_3O_4/SeO_x$, $MnO/Mn_3O_4/SeO_x$ and Mn_3O_4/SeO_x hybrids (the surface detection depth is about 10 nm) are shown in Fig. 5. Figure 5(a) shows that the full survey spectra for the hybrids all contain the characteristic peaks of Mn 2p, Mn 3s, Mn 3p and O 1s. Moreover, the $Mn_2O_3/Mn_3O_4/SeO_x$ hybrid contains the characteristic peak of Se. Figure 5(b) shows the close inspection of Fig. 5(a), indicating that for $Mn_2O_3/Mn_3O_4/SeO_x$ hybrid the characteristic peaks of Se 3s, Se 3p and Se 3d are observed [19]. Figure 5(c) shows the high-resolution XPS spectrum of Se 3d for the $Mn_2O_3/Mn_3O_4/SeO_x$ hybrid, the two notable peaks at 59.4 and 58.6 eV

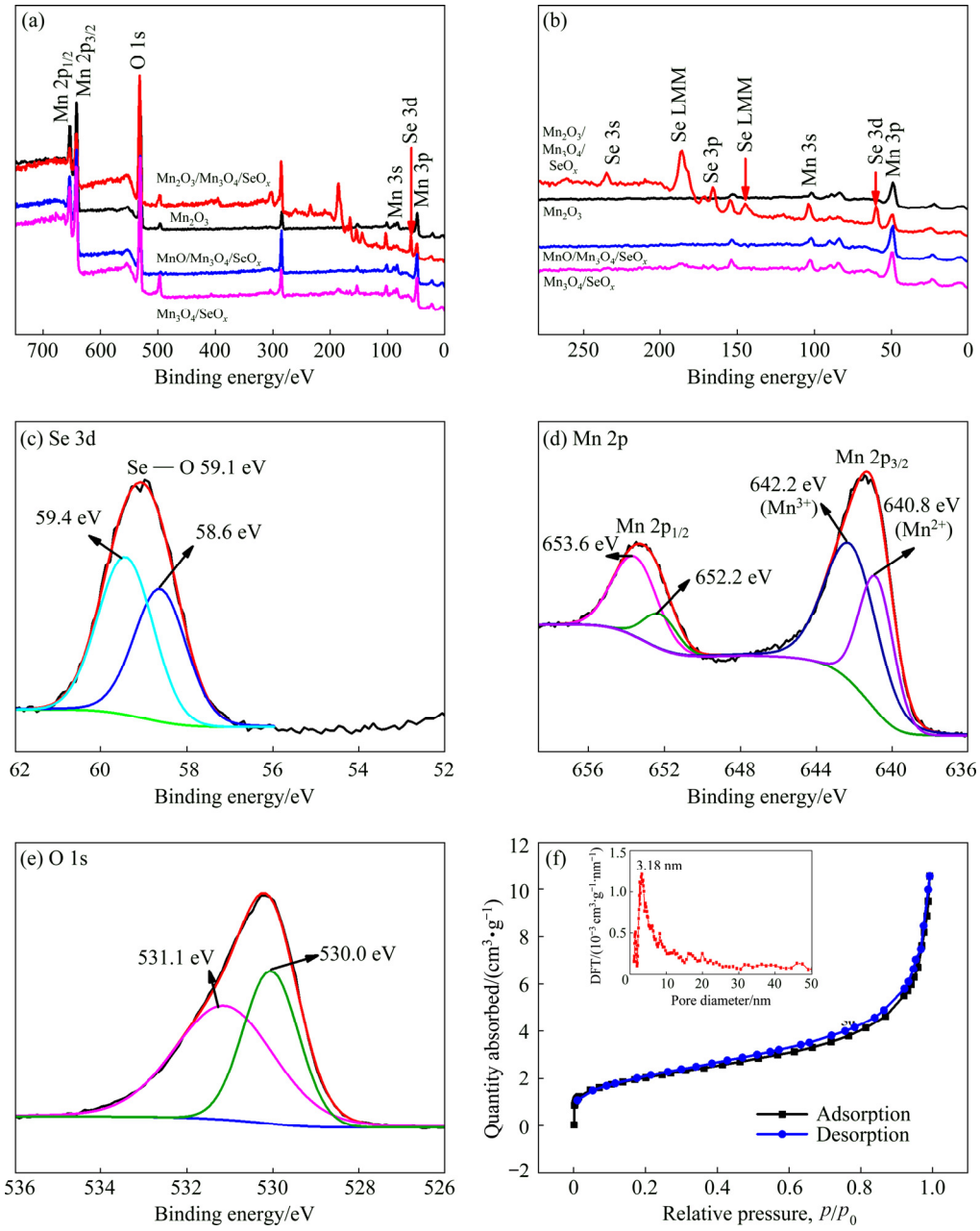

Fig. 5 XPS spectra of Mn_2O_3, $Mn_2O_3/Mn_3O_4/SeO_x$, $MnO/Mn_3O_4/SeO_x$ and Mn_3O_4/SeO_x hybrids (a), close inspection of (a) (b), high-resolution XPS spectrum of $Mn_2O_3/Mn_3O_4/SeO_x$ hybrid for Se 3d (c), high-resolution XPS spectrum of $MnO/Mn_3O_4/SeO_x$ hybrid for Mn 2p (d), high-resolution XPS spectrum of $MnO/Mn_3O_4/SeO_x$ hybrid for O 1s (e) and BET isotherm plots and corresponding pore size distributions (inset) of $MnO/Mn_3O_4/SeO_x$ hybrid (f)

are corresponding to Se^{4+} [20]. The high-resolution XPS spectrum of Mn 2p for the $MnO/Mn_3O_4/SeO_x$ hybrid in Fig. 5(d) shows two distinct peaks at 653.6 and 642.2 eV, respectively, which are in good agreement with the reported results of Mn_3O_4 [4]. All these results indicate that the main phase in the surface for the $MnO/Mn_3O_4/SeO_x$ hybrid is Mn_3O_4, which is consistent with the TEM results. Figure 5(e) shows the high-resolution XPS spectrum of O 1s for the $MnO/Mn_3O_4/SeO_x$ hybrid, in which the distinct peaks at 531.1 and 530.0 eV can be ascribed to Mn—O—Mn and Mn—O bonds, respectively [16]. The specific surface area of the $MnO/Mn_3O_4/SeO_x$ hybrid is found to be 6.18 m^2/g (Fig. 5(f)). The pore size distribution (the inset in Fig. 5(f)) calculated from the DFT method shows an average pore size of 3.18 nm, and the total pore volume is calculated to be 0.011 cm^3/g. The mesoporous structure is favorable for electrolyte penetration in the $MnO/Mn_3O_4/SeO_x$ hybrid.

Figure 6(a) shows the cyclic voltammetry (CV) curves of the $MnO/Mn_3O_4/SeO_x$ electrode for the

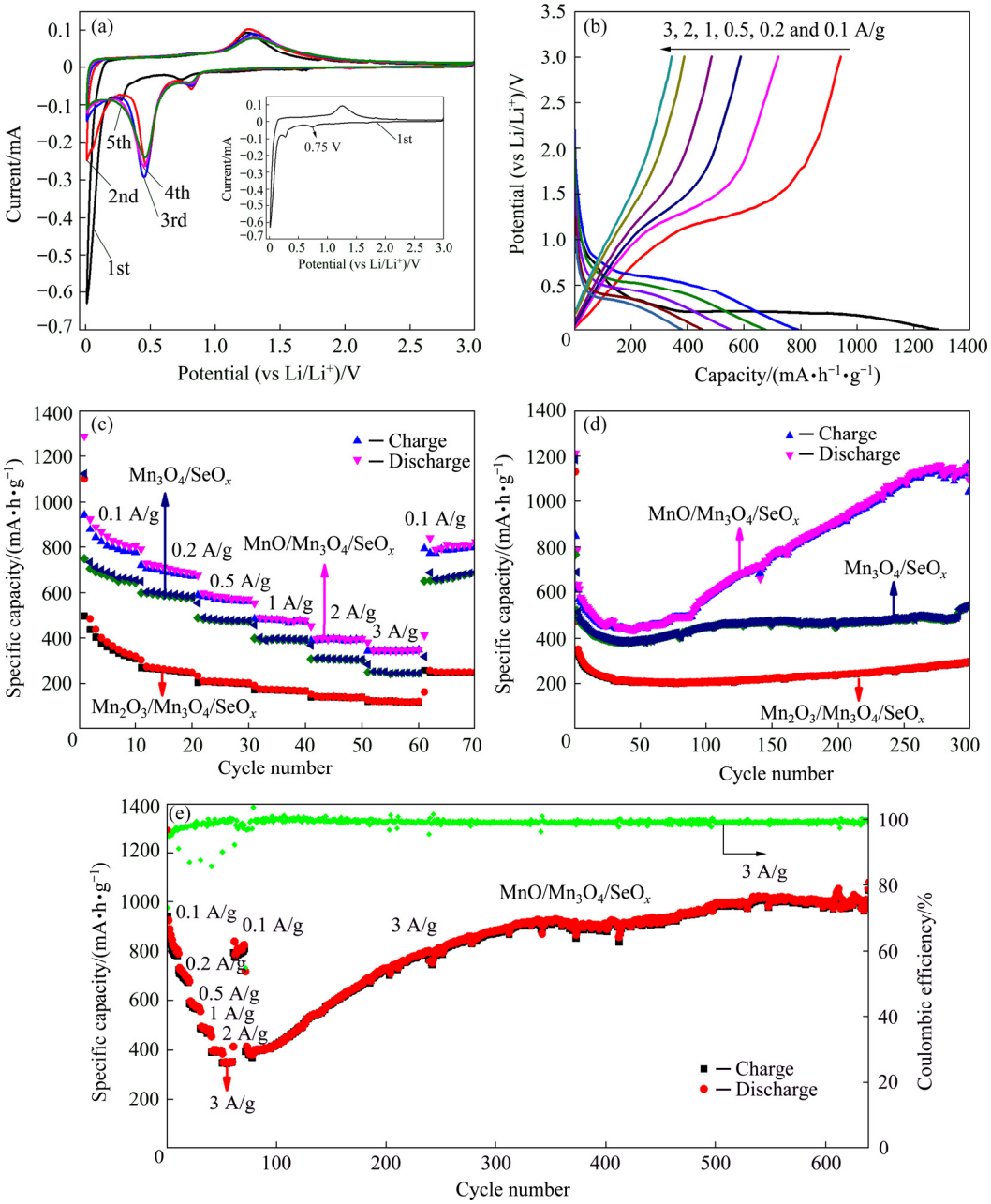

Fig. 6 Cyclic voltammetry curves of $MnO/Mn_3O_4/SeO_x$ electrode (inset shows the first cyclic voltammetry curve) (a), charge/discharge curves of $MnO/Mn_3O_4/SeO_x$ electrode (b), rate performance of $Mn_2O_3/Mn_3O_4/SeO_x$, $MnO/Mn_3O_4/SeO_x$ and Mn_3O_4/SeO_x electrodes (c), cycling performance of $Mn_2O_3/Mn_3O_4/SeO_x$, $MnO/Mn_3O_4/SeO_x$ and Mn_3O_4/SeO_x electrodes at 1 A/g (d) and cycling performance and coulombic efficiency of $MnO/Mn_3O_4/SeO_x$ electrode at current densities of 0.1−3 A/g (e)

initial five cycles at a scan rate of 0.1 mV/s. As shown in the insert of Fig. 6(a), in the initial cathodic process, there is a wide reduction peak at around 0.75 V due to the formation of a solid–electrolyte interface (SEI) film. Furthermore, two main lithiation peaks centered at around 0.28 and below 0.20 V can be attributed to the reduction of Mn^{3+} to Mn^{2+} and Mn^0, respectively (Mn_3O_4+ $2Li^+$+2e→3MnO+Li_2O, MnO+$2Li^+$+2e ⇌ Mn+ Li_2O) [21]. Due to the improved reaction kinetics after the first lithiation, the reduction peak shifted to higher potentials of around 0.82 and 0.46 V for the second and following cycles, respectively. The broad oxidation peak located at around 1.25 V in the reverse sweep during the anodic process is ascribed to the reoxidation of metallic Mn [21]. The charge/discharge profiles at different current densities are displayed in Fig. 6(b). The distinct plateaus in the discharge/charge profiles are in accordance with the CV curves. The first discharge and charge capacities are 1287 and 941 mA·h/g, respectively. The initial irreversible capacity loss (~27.1%) can be ascribed to the formation of the SEI layer and the incomplete conversion reaction [22].

The rate performance of the prepared electrodes was evaluated in the current density range from 0.1 to 3 A/g (Fig. 6(c)). For the $MnO/Mn_3O_4/SeO_x$ electrode, the average reversible discharge capacities are found to be 828, 716, 589, 490, 402 and 350 mA·h/g as the current densities are increased from 0.1, 0.2, 0.5, 1, 2 and 3 A/g, respectively. Moreover, when the current density is restored to 0.1 A/g, the capacity also recovers to 793 mA·h/g, which indicates an excellent reversibility of the electrode. The rate performance of the $MnO/Mn_3O_4/SeO_x$ electrode is obviously higher than that of the $Mn_2O_3/Mn_3O_4/SeO_x$ (127 mA·h/g at 3 A/g) and Mn_3O_4/SeO_x (24 mA·h/g at 3 A/g) electrodes. The results imply that there are significant synergistic effects between the MnO and Mn_3O_4 in the $MnO/Mn_3O_4/SeO_x$ hybrid. The excellent rate capability benefits from the residual amount of Se in the hybrid and the good interparticle adhesion that can facilitate the electronic transfer. In addition, the grain boundaries formed by MnO and Mn_3O_4 can accelerate the reaction kinetics [17].

To understand the capacity and stability of the prepared electrodes, the test was carried out at a current density of 1 A/g for 300 cycles (Fig. 6(d)). The discharge capacities of the $Mn_2O_3/Mn_3O_4/SeO_x$, $MnO/Mn_3O_4/SeO_x$ and Mn_3O_4/SeO_x electrodes are 300, 1122 and 544 mA·h/g at the 300th cycle, respectively. The discharge capacity of the $MnO/Mn_3O_4/SeO_x$ electrode rapidly drops over the first 45 cycles and decreases to 437 mA·h/g, then gradually increases to 1103 mA·h/g at the 253rd cycle, still reaches as high as 1122 mA·h/g at the 300th cycle. The cycling performance of the $MnO/Mn_3O_4/SeO_x$ electrode has been improved significantly, mainly attributing to the pseudo-capacitance lithium storage behavior, which is excited by the microstructural transformation induced by charge/discharge cycles. After charge/discharge cycles, the capacity of manganese oxides electrodes decreases rapidly, for which the main reason is that all generated Mn^0 has not been reversibly converted to MnO_x [23]. The rising trend of capacity between the 45th and 253rd cycles of the $MnO/Mn_3O_4/SeO_x$ electrode can be reasonably explained by the enhancement of electrochemical activation of active materials [24]. In addition, MnO and Mn_3O_4 phases are changed from a crystal state to an amorphous one during the charge/discharge cycles, and this amorphous structure can increase the void space inside the hybrid and thus enhance the pseudocapacitance effect [25].

In order to explore the cycling stability at high current densities of the $MnO/Mn_3O_4/SeO_x$ electrode, it was firstly tested for 70 cycles at the current densities of 0.1, 0.2, 0.5, 1, 2, 3 and 0.1 A/g, and then tested continuously at a current density of 3 A/g, and the results are shown in Fig. 6(e). The discharge specific capacity decreases to 378 mA·h/g after 78 cycles, and then increases rapidly. The $MnO/Mn_3O_4/SeO_x$ electrode still shows 1007 mA·h/g after 630 cycles, which is higher than the theoretical capacity of MnO (756 mA·h/g) and even that of Mn_3O_4 (936 mA·h/g). All these results show that the $MnO/Mn_3O_4/SeO_x$ electrode also possesses an excellent long-term cycling stability at high current density. To the best of our knowledge, this is the best cycling stability at high current density ever reported for transition metal oxide anode in LIBs. A comparison of the cycling stability and rate capability of the $MnO/Mn_3O_4/SeO_x$ anode with those of the previously reported transition metal oxide anode for LIBs is given in Table 1. At a current density of 3 A/g, the coulombic

Table 1 Comparison of cycling stability and rate capability of $MnO/Mn_3O_4/SeO_x$ anodes with previously reported transition metal oxide anodes for LIBs

Transition metal oxide anode	Specific discharge capacity/(mA·h·g^{-1})	Current density/(A·g^{-1})	Total cycle number	Specific capacity at high current density/(mA·h·g^{-1})	Ref.
Spherical α-Fe_2O_3	968	0.1	100	631 at 1.6 A/g after 50 cycles	[26]
3D mesoporous Co_3O_4 networks	957	0.2	200	485 at 5 A/g after 700 cycles	[27]
NiO nanosheets	675	0.359	40	755 at 3.59 A/g after 20 cycles	[28]
3D hierarchical Co_3O_4/CuO nanowire arrays	1191	0.2	200	810 at 1 A/g after 500 cycles	[29]
Fe_2O_3@Co_3O_4 nanowire array	1005.1	0.2	50	788.9 at 5 A/g after 25 cycles	[30]
Porous Co_3O_4@TiO_2 core−shell nanofibers	525	0.445	100	359.3 at 1.78 A/g after 50 cycles	[31]
NiO–Co_3O_4 nanoplate composite	633	0.1	70	600 at 0.4 A/g after 150 cycles	[32]
Fe_2O_3@$NiCo_2O_4$ porous nanocages	1079.6	0.1	100	661.8 at 1 A/g after 40 cycles	[33]
Porous Mn_2O_3	705	1.0	250	450 at 4 A/g after 50 cycles	[34]
$ZnMn_2O_4$ microspheres	1132	0.5	500	596 at 2 A/g after 550 cycles	[35]
$MnO/Mn_3O_4/SeO_x$	1122	1.0	300	1007 at 3 A/g after 560 cycles	This work

efficiency of the $MnO/Mn_3O_4/SeO_x$ electrode increases to 97.8% for the third charge/discharge cycle, and then exceeds 98.5% until the end of the charge/discharge cycles, indicating an excellent stability of the generated SEI film [22].

Figure 7 displays the Nyquist plots of the Mn_2O_3, $Mn_2O_3/Mn_3O_4/SeO_x$, $MnO/Mn_3O_4/SeO_x$ and Mn_3O_4/SeO_x electrodes. The equivalent circuit for EIS fitting is presented by the inset in Fig. 7, where R_Ω is the ohmic resistance, R_{ct} corresponds to the charge–transfer resistance, Z_W is the Warburg impedance, and C_d is the double-layer capacitance [36]. The semicircle from high to medium frequencies is associated with the R_{ct}, as can be seen from Fig. 7, the R_{ct} of the electrode decreases significantly for the hybrids prepared after thermal annealing with Se. The fitting analysis of the test results was carried out for the Mn_2O_3, $Mn_2O_3/Mn_3O_4/SeO_x$, $MnO/Mn_3O_4/SeO_x$ and Mn_3O_4/SeO_x electrodes, yielding corresponding R_{ct} values of 52.4, 28.9, 25.3 and 18.5 Ω, respectively; and R_Ω values of 1.94, 1.73, 1.85 and 1.79 Ω, respectively. These results show that the R_{ct} values

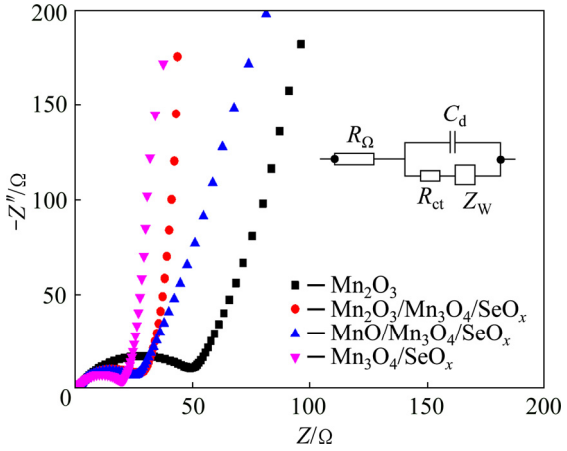

Fig. 7 Nyquist plots of Mn_2O_3, $Mn_2O_3/Mn_3O_4/SeO_x$, $MnO/Mn_3O_4/SeO_x$ and Mn_3O_4/SeO_x electrodes

of the electrodes containing Se decrease significantly, which is mainly attributed to the fact that the residual Se in the hybrids could improve the interfacial conductivity [16]. The electronic conductivity of Mn_3O_4 is higher than that of MnO, so the charge-transfer resistance of the Mn_3O_4/SeO_x electrode is much smaller than that of the $MnO/Mn_3O_4/SeO_x$ electrode [18]. However, the rate

capability and cycling stability of $MnO/Mn_3O_4/SeO_x$ electrode are superior to those of the Mn_3O_4/SeO_x electrode, because the phase boundaries between MnO and Mn_3O_4 are beneficial to the acceleration of Li^+ diffusion [17].

TEM was utilized to characterize the microstructure of the $MnO/Mn_3O_4/SeO_x$ hybrid after 1000 cycles at 3 A/g, and the results are shown in Fig. 8. Figures 8(a) and (b) clearly illustrate the microstructural feature showing the submicron particles adhered tightly to each other, which is in good agreement with the TEM images in Figs. 4(a) and (b). However, the particle size is reduced obviously (i.e. reduced from more than 200 nm to less than 100 nm), indicating that particle pulverization occurs after charge/discharge cycles. With the decrease of particle size, much larger surface area can be formed, and the smaller particles and the formation of defects in the electrode improve the reaction kinetics, resulting in a lower overpotential of Mn^{2+} to Mn^{3+}. It can also be clearly observed from the high-resolution TEM image in Fig. 8(c) that most of the areas show an amorphous feature, and a few numbers of small grains exist (the areas within the four white dotted circles). The surface and internal structures of amorphous manganese oxides are changed due to the disordered distribution of both manganese atoms and oxygen atoms in the hybrid, and the disordered structure can increase the void space in the hybrid to accelerate the reaction kinetics [37].

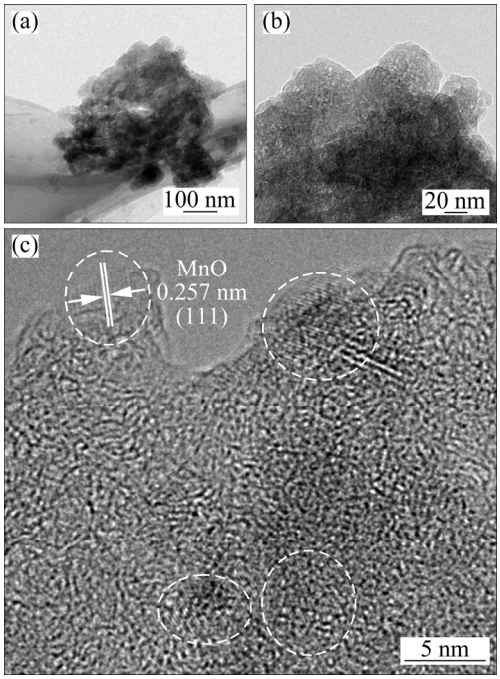

Fig. 8 TEM image of $MnO/Mn_3O_4/SeO_x$ hybrid after 1000 cycles at 3 A/g (a), high-magnification image of (a) (b) and high-resolution image of (b) (c)

According to previous reports, larger surface area can be formed with the decrease of particle size for the $MnO/Mn_3O_4/SeO_x$ hybrid during the cycling process, so that these ample interfaces could possibly result in an increase of pseudocapacitive capacity. Thus, we further analyzed the kinetics of the $MnO/Mn_3O_4/SeO_x$ electrode by CV. Figure 9(a) shows the CV curves of a fresh $MnO/Mn_3O_4/SeO_x$ electrode at various scan rates from 0.1 to 2.0 mV/s. The pseudocapacitive contribution can be qualitatively analyzed according to the power-law formula (Eq. (1)). The relationship between peak current (I_p) and scan rate (v) can be calculated by Eq. (2):

$$I_p=av^b \tag{1}$$

$$\lg I_p=b\lg v+\lg a \tag{2}$$

where a and b are adjustable constants [10]. The values of b can be calculated based on the slope of the linear plots of $\lg I_p$ versus $\lg v$. Generally, a value of b close to 0.5 indicates a diffusion-controlled behavior, while a value of b approaching 1.0 infers a capacitive process. From Fig. 9(b), the b values for the cathodic (Peak 1) and anodic (Peak 2) peaks are determined to be 0.81 and 0.75, respectively, indicating that the electrochemical reactions of the $MnO/Mn_3O_4/SeO_x$ electrode are mainly controlled by the pseudocapacitive behavior. The pseudocapacitive contribution can further be calculated according to Eq. (3) or (4)) [10]

$$I(V)=k_1v+k_2v^{1/2} \tag{3}$$

$$I(V)/v^{1/2}=k_1v^{1/2}+k_2 \tag{4}$$

where k_1 and k_2 are constants for a given potential, and k_1v and $k_2v^{1/2}$ represent the corresponding current response I at a given fixed potential V originated from the pseudocapacitive effects and the diffusion-controlled Li^+-insertion reactions, respectively. As shown in Fig. 9(c), the fresh $MnO/Mn_3O_4/SeO_x$ electrode displays a 61.5% for the pseudocapacitive contribution at a scan rate of 0.1 mV/s, and gradually improves to 89.5% at 2.0 mV/s. The high pseudocapacitance contribution is mainly attributed to the amorphous state of manganese oxides [9].

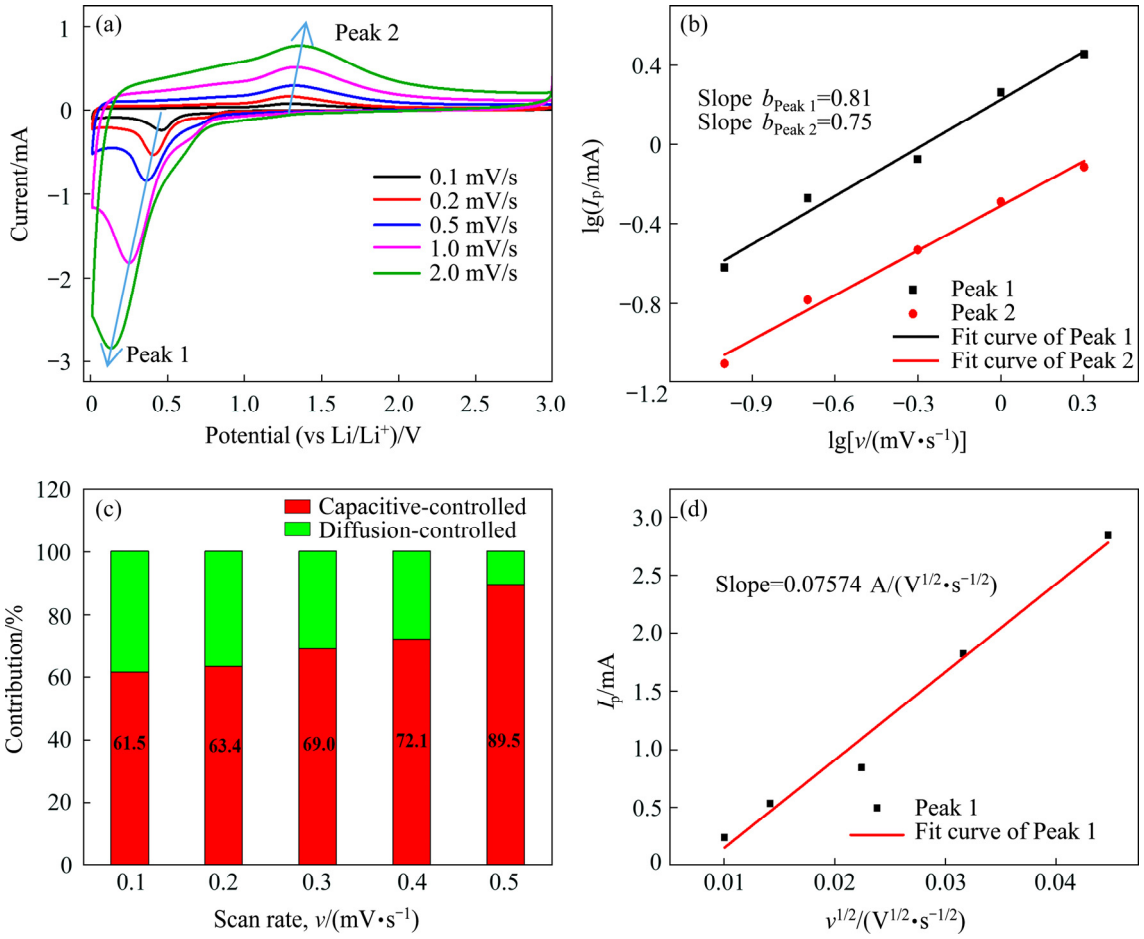

Fig. 9 Cyclic voltammetry curves of $MnO/Mn_3O_4/SeO_x$ electrode at various scan rates (a), lg I_p versus lg v plots of different cathodic/anodic peaks (b), normalized contribution ratios of capacitive and diffusion-controlled capacities at different scan rates (c), and relationship between I_p and $v^{1/2}$ for $MnO/Mn_3O_4/SeO_x$ electrode (d)

According to a series of CV test results at various scan rates, the kinetics of Li^+ diffusion inside the $MnO/Mn_3O_4/SeO_x$ electrode was also investigated, and the results are shown in Fig. 9(d). The Li^+ diffusion coefficient is calculated based on the Randles–Sevcik equation ((Eq. (5)) [38]:

$$I_p=2.69\times10^5 n^{3/2} A D^{1/2} C_0 v^{1/2} \quad (5)$$

where I_p is the peak current (A), n is the electron transfer number (Li^+, n=1), A is the electrode area (1.13 cm^2 in this work), D is Li^+ diffusion coefficient (D_{Li^+}, cm^2/s), C_0 is the Li^+ concentration in electrolyte (mol/L), and v is scan rate (V/s). According to linear fitting results of I_p and $v^{1/2}$ and Eq. (5), D_{Li^+} in the $MnO/Mn_3O_4/SeO_x$ electrode is estimated to be 6.2×10^{-8} cm^2/s, which is five orders of magnitude higher than that of manganese oxide nanowire [39].

4 Conclusions

(1) A $MnO/Mn_3O_4/SeO_x$ hybrid anode material was prepared by a method of precipitation combined with thermal annealing.

(2) The residual amount of Se in the hybrid and the strong interparticle adhesion are beneficial to the electron transfer, which improve the conversion reaction rate and efficiency.

(3) The $MnO/Mn_3O_4/SeO_x$ electrode delivered an excellent cycling performance (1007 mA·h/g at 3 A/g after 560 cycles).

(4) The manganese oxides were gradually transformed from a crystalline state to an amorphous form during the charge/discharge cycles, thus forming much more interfaces and void spaces in the hybrid, which resulted in an increase of pseudocapacitance capacity to 89.5% at 2.0 mV/s.

References

[1] LI M, LU J, CHEN Z W, AMINE K. 30 years of lithium-ion batteries [J]. Advanced Materials, 2018, 30: 1800561.

[2] ZENG Jing, PENG Chao-qun, WANG Ri-chu, LIU Ya-jing, WANG Xiao-feng, LIU Jun. Preparation of dual-shell Si/TiO_2/CFs composite and its lithium storage performance [J]. Transactions of Nonferrous Metals Society of China, 2019, 29(11): 2384−2391.

[3] GALLAGHER K G, TRASK S E, BAUER C, WOEHELE T, LUX S F, TSCHECH M, LAMP P, POLZIN B J, HA S, LONG B, WU Q L, LU W Q, DEES D W, JANSEN A N. Optimizing areal capacities through understanding the limitations of lithium-ion electrodes [J]. Journal of the Electrochemical Society, 2016, 163: A138−A149.

[4] LI Lie-wu, WANG Li-ping, ZHANG Ming-yu, HUANG Qi-zhong, CHEN Li-bao, WU Fei-xiang. High-performance lithium-ion battery anodes based on Mn_3O_4/nitrogen-doped porous carbon hybrid structures [J]. Journal of Alloys and Compounds, 2019, 775: 51−58.

[5] AN Chang-sheng, YUAN Yi-fei, ZHANG Bao, TANG Lin-bo, XIAO Bin, HE Zhen-jiang, ZHENG Jun-chao, LU Jun. Graphene wrapped $FeSe_2$ nano-microspheres with high pseudocapacitive contribution for enhanced Na-ion storage [J]. Advanced Energy Materials, 2019, 9: 1900356.

[6] LEE S W, YABUUCHI N, GALLANT B M, CHEN S, KIM B S, HAMMOND P T, SHAO−HORN Y. High-power lithium batteries from functionalized carbon-nanotube electrodes [J]. Nature Nanotechnology, 2010, 5: 531−537.

[7] AUGUSTYN V, COME J, LOWE M A, KIM J W, TABERNA P L, TOLBERT S H, ABRUNA H D, SIMON P, DUNN B. High-rate electrochemical energy storage through Li^+ intercalation pseudocapacitance [J]. Nature Materials, 2013, 12: 518−522.

[8] JIANG Y Z, ZHANG D, LI Y, YUAN T Z, BAHLAWANE N, LIANG C, SUN W P, LU Y H, YAN M. Amorphous Fe_2O_3 as a high-capacity, high-rate and long-life anode material for lithium ion batteries [J]. Nano Energy, 2014, 4: 23−30.

[9] YUAN Tian-zhi, JIANG Yin-zhu, SUN Wen-ping, XIANG Bo, LI Yong, YAN Mi, XU Ben, DOU Shi-xue. Ever-increasing pseudocapacitance in RGO−MnO−RGO sandwich nanostructures for ultrahigh-rate lithium storage [J]. Advanced Functional Materials, 2016, 26: 2198−2206.

[10] YUAN Tian-zhi, JIANG Yin-zhu, WANG Qiu-ting, PAN Bin, YAN Mi. Pseudocapacitance-enhanced high-rate lithium storage in “honeycomb”-like Mn_2O_3 anodes [J]. Chem Electro Chem, 2017, 4: 565−569.

[11] FANG Guo-zhao, WANG Qi-chen, ZHOU Jiang, LEI Yong-peng, CHEN Zi-xian, WANG Zi-qing, PAN An-qiang, LIANG Shu-quan. Metal organic framework-templated synthesis of bimetallic selenides with rich phase boundaries for sodium-ion storage and oxygen evolution reaction [J]. ACS Nano, 2019, 13: 5635−5645.

[12] ZHOU Peng, CHEN Li-bao, ZHANG Ming-yu, HUANG Qi-zhong, CUI Chao, LI Xiu, WANG Li-ping, LI Lie-wu, YANG Cheng, LI Yu-hao. Embedding α-MnSe nanodots in nitrogen-doped electrospinning carbon nanofibers to enhanced storage properties of lithium-ion batteries [J]. Journal of Alloys and Compounds, 2019, 797: 826−833.

[13] PARK G D, HONG J H, CHOI J H, LEE J H, KIM Y S, KANG Y C. Synthesis process of $CoSeO_3$ microspheres for unordinary Li-ion storage performances and mechanism of their conversion reaction with Li ions [J]. Small, 2019, 15: 1901320.

[14] LI Lie-wu, WANG Li-ping, ZHANG Ming-yu, HUANG Qi-zhong. Formation of Mn−Cr mixed oxide nanosheets with enhanced lithium storage properties [J]. RSC Advances, 2018, 8: 29670−29677.

[15] DENG Yuan-fu, LI Zhan-en, SHI Zhi-cong, XU Hui, PENG Feng, CHEN Guo-hua. Porous Mn_2O_3 microsphere as a superior anode material for lithium ion batteries [J]. RSC Advances, 2012, 2: 4645−4647.

[16] ZHAO Xiao-sen, YIN Li-chang, ZHANG Tong, ZHANG Min, FANG Zhi-bo, WANG Chun-zhong, WEI Ying-jin, CHENG Gang, ZHANG Dong, SUN Zhen-hua, LI Feng. Heteroatoms dual-doped hierarchical porous carbon−selenium composite for durable Li−Se and Na−Se batteries [J]. Nano Energy, 2018, 49: 137−146.

[17] ZHOU Han, LI Zhao-yang, WANG Ke, GAO Meng-qiu, DING Shu-jiang. Phase boundary-enhanced Ni_3N−Co_3N@CNT composite materials for lithium-ion batteries [J]. Journal of Materials Chemistry A, 2019, 7: 1779−1784.

[18] WANG Chang-bin, YIN Long-we, XIANG Dong, QI Yong-xin. Uniform carbon layer coated Mn_3O_4 nanorod anodes with improved reversible capacity and cyclic stability for lithium ion batteries [J]. ACS Applied Materials & Interfaces, 2012, 4: 1636−1642.

[19] YANG X M, WANG S, YU D Y W, ROGACH A L. Direct conversion of metal−organic frameworks into selenium/selenide/carbon composites with high sodium storage capacity [J]. Nano Energy, 2019, 58: 392−398.

[20] HE Qian, LI Shuo-lin, HUANG Shao-wei, XIAO Long-qiang, HOU Lin-xi. Construction of uniform Co−Sn−X (X=S, Se, Te) nanocages via anion exchange reaction with enhanced photovoltaics and oxygen evolution properties [J]. Nanoscale, 2018, 10: 22012−22024.

[21] WANG Jian-gan, JIN Dan-dan, ZHOU Rui, LI Xu, LIU Xing-rui, SHEN Chao, XIE Ke-yu, LI Bao-hua, KANG Fei-yu, WEI Bing-qing. Highly flexible graphene/Mn_3O_4 nanocomposite membrane as advanced anodes for LI-ion batteries [J]. ACS Nano, 2016, 10: 6227−6234.

[22] JIN Y, LI S, KUSHIMA A, ZHENG X Q, SUN Y M, XIE J, SUN J, XUE W J, ZHOU G M, WU J, SHI F F, ZHANG R F, ZHU Z, SO K, CUI Y, LI J. Self-healing SEI enables full−cell cycling of a silicon-majority anode with a coulombic efficiency exceeding 99.9% [J]. Energy & Environmental Science, 2017, 10: 580−592.

[23] LIU Rui, ZHAO Shi-qiang, ZHANG Miao-miao, FENG Fan, SHEN Qiang. High interfacial lithium storage capability of hollow porous Mn_2O_3 nanostructures obtained from carbonate precursors [J]. Chemical Communications, 2015, 51: 5728−5731.

[24] HU Y Y, LIU Z G, NAM K W, BORKIEICZ O J, CHENG J, HUA X, DUNSTAN M T, YU X Q, WIADEREK K M, DU L S, CHAPMAN K W, CHUPAS P J, YANG X Q, GREY C

P. Origin of additional capacities in metal oxide lithium-ion battery electrodes [J]. Nature Materials, 2013, 12: 1130−1136.

[25] LIAN Qing-wang, ZHOU Gang, LIU Jia-tu, WU Chen, WEI Wei-feng, CHEN Li-bao, LI Cheng-chao. Extrinsic pseudocapacitve Li-ion storage of SnS anode via lithiation-induced structural optimization on cycling [J]. Journal of Power Sources, 2017, 366: 1−8.

[26] SANTHOSHKUMAR P, PRASANNA K, JO Y N, SIVAGAMI I N, KANG S H, LEE C W. A facile and highly efficient short-time homogenization hydrothermal approach for the smart production of high-quality α-Fe_2O_3 for rechargeable lithium batteries [J]. Journal of Materials Chemistry A, 2017, 5: 16712–16721.

[27] ZHU Shan, LI Jia-jun, DENG Xiao-yang, HE Chun-nian, LIU En-zuo, HE Fang, SHI Chun-sheng, ZHAO Nai-qin. Ultrathin-nanosheet-induced synthesis of 3D transition metal oxides networks for lithium ion battery anodes [J]. Advanced Functional Materials, 2017, 27: 1605017.

[28] LIN F, NORDLUND D, WENG T C, ZHU Y, BAN C M, RICHARDS R M, XIN H L. Phase evolution for conversion reaction electrodes in lithium-ion batteries [J]. Nature Communications, 2014, 5: 3358.

[29] WANG Jie-xi, ZHANG Qiao-bao, LI Xin-hai, XU Da-guo, WANG Zhi-xing, GUO Hua-jun, ZHANG Kai-li. Three-dimensional hierarchical Co_3O_4/CuO nanowire heterostructure arrays on nickel foam for high–performance lithium ion batteries [J]. Nano Energy, 2014, 6: 19–26.

[30] XIONG Q Q, XIA X H, TU J P, CHEN J, ZHANG Y Q, ZHOU D, GU C D, WANG X L. Hierarchical Fe_2O_3@Co_3O_4 nanowire array anode for high-performance lithium ion batteries [J]. Journal of Power Sources, 2013, 240: 344–350.

[31] TONG Xiao-ling, ZENG Min, LI Jing, LIU Zhan-jun. Porous Co_3O_4@TiO_2 core-shell nanofibers as advanced anodes for lithium ion batteries [J]. Journal of Alloys and Compounds, 2017, 723: 129–138.

[32] ZHANG Yi-ping, ZHUO Qi-qi, LV Xiao-xin, MA Yan-yun, ZHONG Jun, SUN Xu-hui. NiO–Co_3O_4 nanoplate composite as efficient anode in Li-ion battery [J]. Electrochimica Acta, 2015, 178: 590−596.

[33] HUANG Gang, ZHANG Lei-lei, ZHANG Fei-fei, WANG Li-min. Metal–organic framework derived Fe_2O_3@$NiCo_2O_4$ porous nanocages as anode materials for Li-ion batteries [J]. Nanoscale, 2014, 6: 5509–5519.

[34] BAI Zhong-chao, ZHANG Yao-hui, ZHANG Yu-wen, GUO Chun-li, TANG Bin, SUN Di. MOFs-derived porous Mn_2O_3 as high-performance anode material for Li-ion battery [J]. Journal of Materials Chemistry A, 2015, 3: 5266–5269.

[35] ZENG Jun-song, REN Yan-biao, WANG Sheng-bin, HAO Yu, WU Hao, ZHANG Shi-chao, XING Ya-lan. Hierarchical porous $ZnMn_2O_4$ microspheres assembled by nanosheets for high performance anodes of lithium ion batteries [J]. Inorganic Chemistry Frontiers, 2017, 4: 1730–1736.

[36] HONG Min, SU Yan-jie, ZHOU Chao, YAO Lu, HU Jing, YANG Zhi, ZHANG Li-ying, ZHOU Zhi-hua, HU Nan-tao, ZHANG Ya-fei. Scalable synthesis of γ-Fe_2O_3/CNT composite as high-performance anode material for lithium-ion batteries [J]. Journal of Alloys and Compounds, 2019, 770: 116−124.

[37] CHAE O B, KIM J, PARK I, JEONG H, KU J H, RYU J H, KANG K, OH S M. Reversible lithium storage at highly populated vacant sites in an amorphous vanadium pentoxide electrode [J]. Chemistry of Materials, 2014, 26: 5874−5881.

[38] LU Bin, LIU Jun, HU Ren-zong, WANG Hui, LIU Jiang-wen, ZHU Min. Facile synthesis of self-supported Mn_3O_4@C nanotube arrays constituting an ultrastable and high-rate anode for flexible Li-ion batteries [J]. Journal of Materials Chemistry A, 2017, 5: 8555−8865.

[39] WU M S, CHIANG P C J. Electrochemically deposited nanowires of manganese oxide as an anode material for lithium-ion batteries [J]. Electrochemistry Communications, 2006, 8: 383−388.

利用赝电容效应提高 Se 修饰 MnO/Mn_3O_4 复合负极材料的储锂容量及倍率性能

黎烈武[1]，王丽平[1,2]，张明瑜[1]，黄启忠[1]，何克坚[3]，吴飞翔[4]

1. 中南大学 粉末冶金国家重点实验室，长沙 410083；2. 长沙学院 生物与环境工程学院，长沙 410022；
3. 中南大学 高等研究中心，长沙 410083；4. 中南大学 冶金与环境学院，长沙 410083

摘 要：为了提高锰氧化物负极材料的倍率和循环性能，采用沉淀法及热处理法，通过调控 Mn_2O_3 与 Se 粉的反应温度，制备 $MnO/Mn_3O_4/SeO_x$ (x=0, 2)复合负极材料。$MnO/Mn_3O_4/SeO_x$ 负极在 3 A/g 电流密度下经过 560 次充放电循环后放电比容量为 1007 mA·h/g。循环伏安法定量分析结果表明，在 2.0 mV/s 的扫描速率下赝电容贡献率高达 89.5%。研究结果表明，MnO 与 Mn_3O_4 之间存在明显的协同效应。

关键词：锂离子电池；锰氧化物；负极材料；赝电容效应；协同效应

(Edited by Wei-ping CHEN)